Permafrost and Periglacial Processes

WILEY

RESEARCH ARTICLE

A Third of Organic Carbon Is Mineral Bound in Permafrost Sediments Exposed by the World's Largest Thaw Slump, Batagay, Siberia

Maxime Thomas[1] | Loeka L. Jongejans[2,3] | Jens Strauss[2] | Chloé Vermylen[1] | Sacha Calcus[1] | Thomas Opel[4] | Alexander Kizyakov[5] | Sebastian Wetterich[2] | Guido Grosse[2,3] | Sophie Opfergelt[1]

[1]Earth and Life Institute, Université catholique de Louvain, Louvain-la-Neuve, Belgium | [2]Permafrost Research Section, Alfred Wegener Institute Helmholtz Centre for Polar and Marine Research, Potsdam, Germany | [3]Institute of Geosciences, University of Potsdam, Potsdam, Germany | [4]Polar Terrestrial Environments Section, Alfred Wegener Institute Helmholtz Centre for Polar and Marine Research, Potsdam, Germany | [5]Cryolithology and Glaciology Department, Faculty of Geography, Lomonosov Moscow State University, Moscow, Russia

Correspondence: Maxime Thomas (maxime.thomas@uclouvain.be)

Received: 28 June 2023 | **Revised:** 3 April 2024 | **Accepted:** 26 April 2024

Funding: This project received funding from the European Union's Horizon 2020 research and innovation program under grant agreement No. 714617 to S.O. (WeThaw), and S.O. acknowledges funding from the Fund for Scientific Research FNRS in Belgium (FC69480). Further funding for this work came from the Leverhulme Trust (Research Project Grant RPG-2020-334) and the AWI baseline funds for the expedition Batagay 2019. L.J. acknowledges the German Federal Environmental Foundation (DBU; project name: "Organic matter stored in ice-rich permafrost: future permafrost thaw and greenhouse gas release").

Keywords: Batagay | headwall | iron | mineral–organic carbon interactions | retrogressive thaw slumps | thermo-erosion

ABSTRACT

Organic carbon (OC) in permafrost interacts with the mineral fraction of soil and sediments, representing <1% to ~80% of the total OC pool. Quantifying the nature and controls of mineral–OC interactions is therefore crucial for realistic assessments of permafrost-carbon-climate feedbacks, especially in ice-rich regions facing rapid thaw and the development of thermo-erosion landforms. Here, we analyzed sediment samples from the Batagay megaslump in East Siberia, and we present total element concentrations, mineralogy, and mineral–OC interactions in its different stratigraphic units. Our findings indicate that up to 34 ± 8% of the OC pool interacts with mineral surfaces or elements. Interglacial deposits exhibit enhanced OC–mineral interactions, where OC has undergone greater microbial transformation and has likely low degradability. We provide a first-order estimate of ~12,000 tons of OC mobilized annually downslope of the headwall (i.e., the approximate mass of 30 large aircrafts), with a maximum of 38% interacting with OC via complexation with metals or associations to poorly crystalline iron oxides. These data imply that over one-third of the OC exposed by the slump is not readily available for mineralization, potentially leading to prolonged OC residence time in soil and sediments under stable physicochemical conditions.

1 | Introduction

Recent studies have shown that, due to the Arctic amplification, air temperature increase is occurring nearly four times faster in the Arctic than the global average increase since 1979 [1]. Ice-rich permafrost is particularly sensitive to warming and subsequent rapid thaw process (e.g., [2–4]) and contains thousands of years old organic carbon (OC), which can be mobilized by various thaw processes (e.g., [5–12]). This OC pool in the northern permafrost-affected regions is estimated to range from 1460- to 1600-Pg carbon (i.e., roughly half of the global soil carbon pool and twice as much as the carbon currently stored in the atmospheric pool; [13, 14]). Existing estimates indicate that 5%–15% of the terrestrial OC reservoir would be

vulnerable to being emitted as greenhouse gases by the end of this century [9, 15], inducing a positive permafrost-carbon-climate feedback. These assessments are based on simulated volumes of OC that will be exposed by the increase in thickness of the seasonally thawing active layer, by a process commonly referred to as gradual thawing. Rapid thaw processes such as thermokarst, thermo-denudation, and thermo-erosion may account for additional release of OC and greenhouse gases not yet accounted for in models simulating gradual thaw [4, 10]. Various factors determine how much of the thawed OC eventually is transformed into greenhouse gases, such as microbial activity (e.g., [16]), soil hydrology and redox state (e.g., [17, 18]), and OC sources and quality (e.g., [19, 20]). The future trajectory of permafrost carbon emissions yet also depends on the proportion of the free OC pool relative to the proportion of mineral-interacting forms of OC [21], as well as the potential contribution of previously perennially frozen deep carbon as a consequence of ice-rich permafrost thaw [22].

By contrast to gradual thaw that occurs across the Arctic, physical degradation of ice-rich permafrost are more punctual events in both time and space, which is why they are sometimes referred to as abrupt thaw events. Such physical degradations—named thermokarst landforms [23, 24]—are the consequence of ground collapse and subsidence caused by the loss of the cementing properties of the melting excess ice in the ground. One of these types of physical degradations are retrogressive thaw slumps (RTS), which are among the most dynamic forms of thermo-erosion and thermo-denudation, sometimes also referred to as hillslope thermokarst [24, 25]. Recent research indicates that under the SSP58.5 scenario (the shared socioeconomic pathway [SSP] corresponding to very high greenhouse gas emissions scenario; [26]), the area susceptible to be affected by hillslope thermokarst landforms is projected to increase by ~250,000 km^2 by the end of the 21st century, but despite the rather small total area, it may account for one-third of all thermokarst-related carbon losses [10]. These phenomena are important to consider in the permafrost carbon budget since this exposed deep OC pool is tens of thousands of years old and would not have re-entered the modern carbon cycle if these disturbances had not occurred, that is, under gradual permafrost thaw. They could significantly increase carbon emissions from thawing permafrost and compromise the feasibility of remaining below 1.5°C or 2°C targeted by the Paris Agreement [22].

Retrogressive thaw slumps are landforms that enlarge due to thawing of frozen deposits and melting of ground ice at a headwall, producing slumping and sediment flow through meltwater streams and mudflows, potentially accumulating in a scar zone or form a mudlobe at the toe of the RTS. Thaw slumping can be initiated, for example, by either lateral or thermal erosion by water [24]; active layer detachment following heavy precipitation [27]; and human activity such as road construction, mining, or deforestation [28]. The retreat of the collapse front each summer can reach several (tens of) meters per year [29–37]. These structures therefore expose and relocate large volumes of material [31, 36, 38–40], such as thawed sediments or melt water, and involve masses of previously perennially frozen carbon in the form of plant and animal remains, until they stabilize. In recent years, increased precipitation in certain Arctic areas has accentuated the development of mega-slumps and downslope sediment transport in debris tongues [31, 41]. These debris tongues can be maintained stable for decades or even centuries [42] and contain OC that is partially bound to minerals (e.g., [43–46]) via OC–mineral interactions.

Soil OC can be conceptualized into a free particulate pool and a pool of mineral-interacting forms of OC [47]. The latter represents a potentially stabilized OC pool with reduced susceptibility to microbial degradation (e.g., [47–52]), which is less likely to contribute to the permafrost-carbon-climate feedback. A recent study has shown that OC in cold regions appears to be distributed mainly in the more vulnerable particulate pool, rather than in the more persistent mineral-interacting pool of OC [48]. Those mineral-interacting forms of OC, however, remain highly variable at the Arctic scale (i.e., accounting for ~1% to ~> 80% of permafrost soils and sediments total OC; [53–55]) and can be divided into three categories: (i) organo-metallic complexes resulting from the complexation of OC with metal ions (i.e., OC complexed with e.g. Al, Fe, Mn; [56, 57]); (ii) organo-mineral associations [50] resulting from the interaction of OC with mineral surfaces (such as OC sorbed onto clay minerals or Fe-oxides, using cation bridges such as Ca or Mg); and (iii) OC physical protection within soil aggregates, which renders OC spatially inaccessible for microorganisms (i.e., occluded, involving clay minerals, Fe-Al (hydr)oxides or carbonates in aggregates; [57]). The free particulate and mineral-interacting forms of organic matter pools are highly contrasted concerning for example their physical and chemical properties, mean residence times in soil, and responses to land use change. It is estimated that particulate organic matter has a mean residence time ranging from a few years to decades, while it persists for decades to centuries for mineral-interacting forms of OC (e.g., [47, 50, 58]). It is worth pointing out that the capability of organic matter to be decomposed also depends on its molecular recalcitrance (i.e., some compounds are inherently stable, e.g., aromatic compounds) but this is thought not to be the dominant mechanism of OC stabilization (e.g., [49, 57]).

Within a thaw slump headwall, the exposed sediments are often stratified into different layers that correspond to different depositional regimes and ages. The environmental conditions at the time of deposition, past permafrost dynamics since deposition and the chemical composition of the sediment will control the nature and amount of OC interacting with the soil/sediments mineral pool. Studying at high vertical resolution the proportion and nature of OC–mineral interactions within such deposits of different ages and lithologic nature is therefore a key step in establishing an enhanced understanding of the carbon balance of material mobilized from such rapid erosion landforms and determining which proportion of the mobilized OC is interacting with the mineral pool as well as the mechanisms involved.

Here, we determine the mechanism for OC–mineral interactions within the sediments of the world's largest known retrogressive thaw slump [32], the Batagay megaslump in East Siberia, exposing the second oldest directly dated permafrost in the Northern Hemisphere (from ~650 ka to the modern day; [59]).

2 | Methods

2.1 | Study Area and Site Description

The Batagay thaw slump, situated about 10 km southeast of Batagay settlement in Yakutia (Figure 1a,b), is located on a northeast-facing hillslope. Based on retrospective remote sensing data analysis; the RTS was formed in the end of 1990s as a bowl-shaped landform [32, 62] at the place of previously existing thermo-erosional gully. The gully and subsequently the slump formed over around 40 years. In 2019, it exposed an about 55-m-high headwall [63, 64]. Following the Köppen [65] climate classification, the area of Batagay is characterized by a subarctic continental climate, which implies relatively low precipitation and a particularly wide seasonal temperature gradient. For a period ranging from 1988 to 2017, the site had a mean winter temperature of −40.0°C (December to February), a mean summer temperature of 13.7°C (July to August), and a mean annual temperature of −12.4°C. For the same period, the mean annual precipitation was 203 mm, and the mean summer precipitation 106 mm [64].

The headwall provides access to frozen stratigraphically discontinuous deposits from the Middle Pleistocene (~650 ky) to the Holocene [59] and consists of six distinct stratigraphic units [59, 64]. Those stratigraphic units have been extensively described in Murton et al. [64]. Briefly, at the slump bottom, the Lower Ice Complex (LIC; ~3–7 m thick) is only exposed at the deepest part of the main headwall and probably still buried for the main part. The LIC developed during the early Middle Pleistocene (MIS 16) or earlier and has survived multiple interglacials, including the super-interglacial MIS 11c. Above the LIC lies the Lower Sand Unit (LSU; ~20 m thick) with horizontally layered sand and thinner ice and composite wedges compared to those of the LIC. The LSU is covered by the Woody Debris layer (WD; MIS 5e), which is laterally discontinuous and present in a few lenses up to 3 m thick, consisting of wood remains with branches and twigs. It is overlain by the Upper Ice Complex (UIC; ~20–25 m thick, MIS 4–2). This is the local equivalent of the late Pleistocene Yedoma ice complex, widespread in Siberia and Alaska, and is dominated by large syngenetic ice wedges embedded within silty and sandy sediments [66]. Total volumetric ice content of the UIC is up to about 87%, of which up to 70.2% is wedge-ice volume [63]. Above the UIC, and only exposed downslope of the main headwall in the northern and southern parts of thaw slump, there is the Upper Sand Unit (USU) of MIS 3 to 2 origin, which was not sampled for this study. Finally, the brown and sandy Holocene Cover (HC) composed of sandy sediments covers the UIC, including a 0.2- to ~1.4-m-thick active layer.

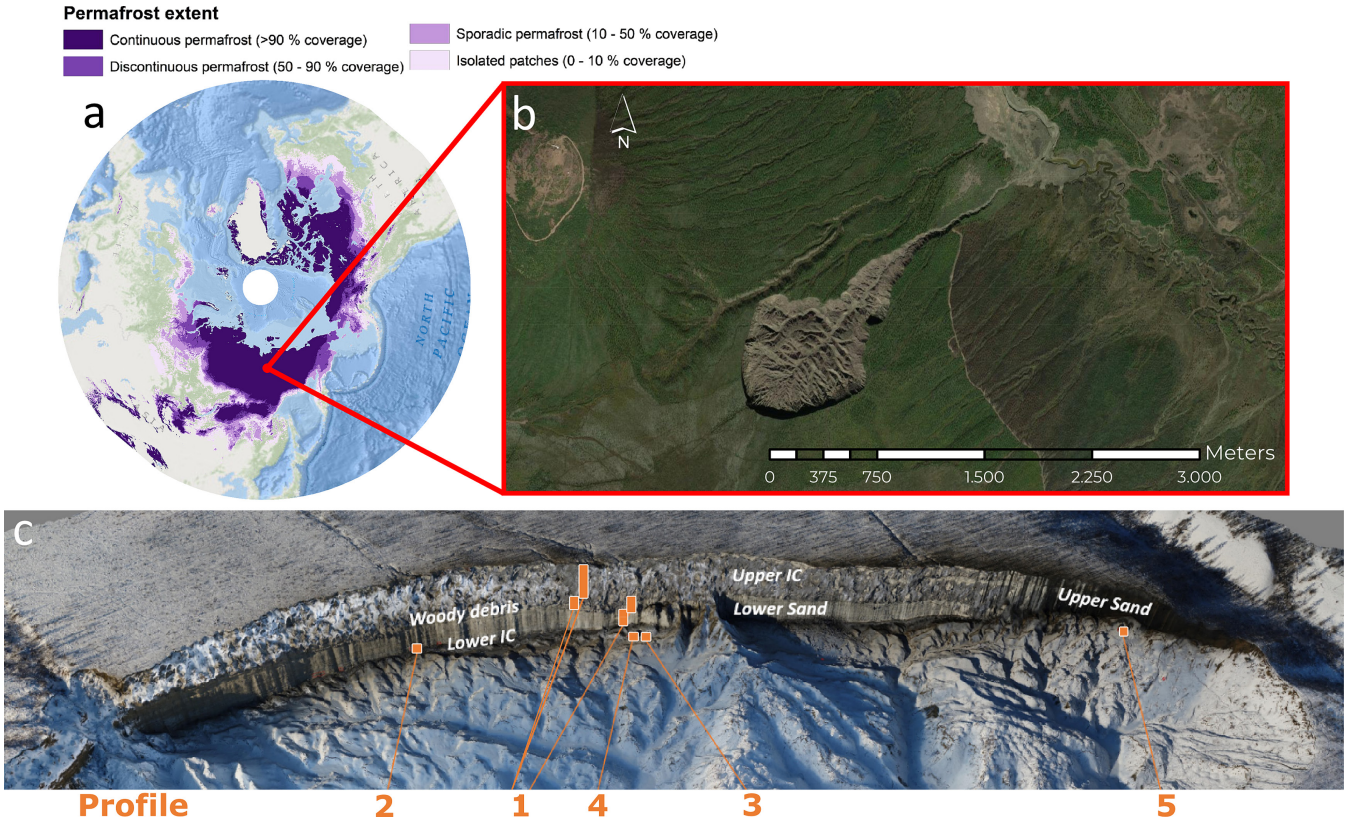

FIGURE 1 | Batagay thaw slump location, extent, morphology, and sampling locations. (a) Permafrost extent in the Northern Hemisphere [60] and (b) thaw slump extent and morphology. Map created in ArcMap 10.8. Basemap layer credits: World Ocean Base in (a): Esri, GEBCO, NOAA, National Geographic, and other contributors. World Imagery in (b): ESRI satellite image basemap; (c) overview of sediments samples at the west wall of the Batagay slump, photo: A. Kizyakov, 24.03.2019. Sediment samples were collected from a main profile (Profile 1). An additional series of sediment samples was taken from the slump bottom (Profile 2), that is, vertically below the main profile. Additional discrete sediment samples were taken in profiles from blocks in the slump bottom (Profiles 3 and 4) and a baydzherakh, that is, a frozen thermokarst mound (Profile 5) (panel c modified from [61]).

The top layer (5 cm) is referred to as the organic layer (OL). In the following, we distinguish (after [20]) between interglacial units comprising the organic layer, the Holocene Cover and Woody Debris layer and units deposited during glacial periods, which are the Upper and Lower Ice Complexes, and the Lower Sand Unit.

2.2 | Sampling Locations

Samples were collected during field work from March 18 to April 4, 2019 [61] along a vertical profile with sample spacing every half a meter for the upper 10 m of the headwall and then every meter due to greater homogeneity beyond 10 m in terms of sedimentology and cryostratigraphy (profile P1, $n = 53$; Figure 1c; Table 1). Sampling was carried out via abseiling from a rope attached to the top of the headwall, using a hole saw (ø57 mm, 40 mm depth) mounted on a Makita power drill. At each sampled depth, three cores were taken next to each other and have already been analyzed for biomarkers and sedimentology in Jongejans et al. [20]. The depths have been calibrated taking into account angles of the wall and rearrangement of the tape-measure and are given in cm below surface. An additional series of samples (profile 2, $n = 7$; Figure 1c; Table 1) was taken from the slump bottom, that is, vertically below the profile P1. These correspond to samples from the LIC (below the thaw unconformity (see Section 2.1) and the LSU. Additional discrete sediment samples were taken in profiles from huge frozen blocks in the slump bottom (Profile 3, $n = 4$; Profile 4, $n = 3$; Figure 1c; Table 1), which could be stratigraphically attributed to their original position in the headwall and a baidzherakh, that is, a frozen thermo-erosional mound (Profile 5, $n = 3$; Figure 1c; Table 1) [20, 61].

2.3 | Mineralogy and Bulk Element Concentrations

The X-ray diffraction (XRD) method allows the characterization of the presence of crystalline mineral phases. This technique is used to determine the atomic and molecular structure of a crystal by analyzing the diffraction pattern produced when X-rays interact with a crystalline material. The diffraction pattern enables the identification of minerals and their relative abundances in the sample. We assessed the mineralogy on finely ground bulk sediments from at least one sample out of two along the profile 1 ($n = 34$), and all samples in profiles 2, 3, 4, and 5 ($n = 17$). The mineralogy of the bulk samples was determined on nonoriented powder finely ground in a mortar (Cu Kα, Bruker Advance D8 diffractometer, detection limit 5% by weight).

We measured the total concentrations of Ca, Fe, Al, and Mn in all samples ($n = 70$) using a portable X-ray fluorescence (XRF) device (*Niton XL3t GOLDD* + pXRF; ThermoFisher Scientific, Waltham, the United States). The measurements were performed in laboratory (ex-situ) conditions on air-dried samples to avoid introduction of additional variability (e.g., water content, sample heterogeneity). Briefly, samples were placed on a circular plastic cap (2.5 cm diameter), its base covered with a thin transparent film (prolene 4 μm). Minimum sample thickness in the cap was set to 2 cm to prevent underestimation of the detected intensities [67], and total time of analysis is set to 90 s to standardize each measurement.

The pXRF-measured concentrations were calibrated using a method following Monhonval et al. [68]. A linear regression was used to correct pXRF concentrations for trueness on all

TABLE 1 | Overview of the number of samples collected, associated depth, stratigraphic unit origin, and age (MIS = marine isotope stages; n = number of samples).

Profile	Stratigraphic units	Age[a]		Depth (cm)	n	Total n
		MIS	ka			
1	Organic layer		Modern	5	1	53
	Holocene Cover	MIS 1	0.39	15–195	6	
	Upper Ice Complex (Yedoma)	MIS 4-2	At least 60 to 30	260–2882	31	
	Woody Debris layer	MIS 5e (last interglaciation)	~125	3012–3259	5	
	Lower Sand Unit	MIS 16-6	~175	3350–4942	10	
2	Lower Sand Unit	MIS 16-6	~175	5100–5150	2	7
	Lower Ice Complex	MIS 16 or earlier	at least 650	5170–5310	5	
3	Upper Ice Complex (Yedoma)				2	4
	Woody Debris layer				2	
4	Woody Debris layer				1	3
	Lower Sand Unit				2	
5	Upper Ice Complex (Yedoma)				3	3
					Total	70

[a]Based on Murton et al. [59].

samples ($n = 70$). This regression was obtained based on element concentrations measured by pXRF and by inductively coupled plasma optical-emission spectrometry (ICP-OES) after alkaline fusion on samples from different permafrost environments, including 13 samples from this study (robust $R^2 \geq 0.9$ for Fe, Ca; robust $R^2 \geq 0.8$ for Mn; robust $R^2 \geq 0.6$ for Al; Figure S1). In the following, the total element concentration measured by XRF and corrected for trueness will be referred to as Ca_t, Mn_t, Al_t, and Fe_t. A complete description of the sites used and the calibrations can be found in the Supporting Information S1.

The total organic carbon (TOC) content on sediments was determined after homogenization of freeze-dried samples using aVario TOC Cube Elemental Analyzer and expressed in wt%, like reported in Jongejans et al. [69]. We acknowledge that the analyses presented in this study focus solely on the soil/sediment fraction of the permafrost samples and not on the organic carbon present, for example, in ice-wedges. In the following, the TOC presented is the TOC present in sediments only.

2.4 | Selective Extractions

Two procedures of selective extraction from soil were used as indicators of the complexed and poorly crystalline oxides phases [70]. More specifically: (i) the sodium pyrophosphate extraction of Fe, Al and Mn targets the organo-metallic complexes [71, 72]. We acknowledge a possible contribution of oxide nanoparticles in addition to the organically-bound metals [56, 73, 74], but limited by centrifugation and filtration of the extract; (ii) the dark ammonium oxalate extraction of Fe targets poorly crystalline oxides (i.e., poorly crystalline oxides and organo-metallic complexes; [75]). The pool of mineral elements that form organo-metallic complexes or associations with OC are often referred to as "reactive". This reactive pool combines all poorly crystalline, amorphous, and complexed forms of Fe, Mn, and Al and corresponds here to the ammonium oxalate extraction.

Those two selective extractions were carried out on at least one sample out of two in the profile 1 ($n = 37$; Figure S2) and all samples in profiles 2, 3, 4, and 5 ($n = 17$). Concentrations in Fe, Al, and Mn were measured in solution by ICP-OES after each selective extraction. In the following, the elements extracted by pyrophosphate and oxalate methods will be referred to as the corresponding element symbol followed by a subscripted letter indicating the type of extraction, namely, "p" for pyrophosphate extraction (Fe_p, Al_p, Mn_p) and "o" for oxalate extraction (Fe_o).

The pool of OC selectively extracted with sodium pyrophosphate [71–73] and dark ammonium oxalate [75] was measured on the same solutions as those used for the selective extractions of metals ($n = 54$; Section 2.5). Briefly, (i) for carbon involved in organo-metallic complexes, we measured dissolved OC released after dispersion by pyrophosphate using a Shimadzu TOC-L analyzer (measuring nonpurgeable OC). In the following, this carbon extracted by pyrophosphate will be referred to as C_p; (ii) for oxalate extracted carbon, we measured the absorbance at 430 nm in the oxalate extract (via a Genesys 10 S VIS spectrophotometer, with the extractant solution as a blank) to evaluate the organic acid concentration. The optical density of the oxalate extract (ODOE) is mainly influenced by the extracted fulvic acids thereby indicating the concentration in organic acids present in the oxalate extract [76].

2.5 | First-Order Estimate of the Material Eroded by the Retreat of the Headwall

Using the sampling depths along the headwall and an estimate of the retreat rate of the collapse front [35], we established a first-order estimate of the annual mass balance assessment of the material eroded from the slump. We first partitioned the wall into horizontal slices using the thickness (m) between different sampling depths, which we multiplied by an average expansion rate of the slump (0.026 km^2/year on average between 1991 and 2018; [35]) to obtain an annual volume of sediment mobilized from each slice. From each slice, we then removed an average volume proportion of ice wedges per stratigraphic unit, following Kizyakov et al. [63], that is, 67% for the Upper Ice Complex, 9% for the Lower Sand Unit, and 56% for the Lower Ice Complex. We then estimated the mass of sediment mobilized annually by each slice by multiplying the annual volume mobilized by the bulk density (Equation 1). The bulk density was determined by using an inverse relationship with porosity, assuming that pore volume in ice-saturated (i.e., > 20% volume) samples is directly measured with pore ice volume (see full method in [77]). If ice content was not measured on the sample, the mean value of the stratigraphic unit was assigned.

$$\begin{aligned} &sediment\ mass\ retreat\ rate\ slice_i \left(\frac{kg_{sediment}}{yr}\right) \\ &= thickness\ slice_i\ (m) \\ &\quad \times \left(1 - ice\ wedge\ volume\ proportion\ slice_i \left(\frac{m^3}{m^3}\right)\right) \\ &\quad \times average\ expansion\ rate \left(\frac{m^2}{yr}\right) \times bulk\ density\ slice_i \left(\frac{kg_{sediment}}{m^3}\right) \end{aligned} \tag{1}$$

To establish the budget for the mobilization of OC and mineral elements as total, complexed and poorly crystalline oxides phases, we multiplied the concentration of each element $\left(\frac{kg_{element}}{kg_{sediment}}\right)$ by the result of Equation (1) $\left(\frac{kg_{sediment}}{yr}\right)$. If the selective extraction was not performed on the sample, the mean value of the stratigraphic unit was assigned. We then summed the contributions from each slice to obtain an estimate of the total mass mobilized each year by the slump for the different elements as total, complexed and poorly crystalline oxides phases (Equation 2).

$$\begin{aligned} &total\ element\ mass\ retreat\ rate \left(\frac{kg_{element}}{yr}\right) \\ &= \sum_{i\ slices} element\ concentration\ slice_i \left(\frac{kg_{element}}{kg_{sediment}}\right) \\ &\quad \times slice_i\ sediment\ mass\ retreat\ rate \left(\frac{kg_{sediment}}{yr}\right) \end{aligned} \tag{2}$$

2.6 | Statistical Analysis

We performed computations for statistical analysis using R software version R.3.6.1 [78]. Compact displays of data distributions were performed using boxplots showing five summary statistics:

the median, two hinges for the 25th and 75th percentiles and two whiskers that extend from the hinges to 1.5 times the inter-quartile range [79, 80]. Robust linear regression (R^2 adj) presented in this study are implemented with an alpha of 0.95. When numerical statistics are presented in the text for dataset descriptions, the mean ± standard deviation of the distribution is presented. For comparing two datasets, we performed nonparametric statistical Wilcoxon test.

3 | Results

3.1 | Mineralogy and Bulk Element Concentrations

In all stratigraphic units, the diffractograms indicate the presence of primary silicate minerals (quartz, pyroxene, sodium-, calcium-, and potassium-feldspars and micas), secondary silicate minerals (kaolinite, illite, vermiculite), sulfates (anhydrite), and, often, carbonates (dolomite). Those mineral species are detected in profile 1 (Figure 2), profile 2 (Figure S3), and profiles 3–4–5 (Figure S4).

Total calcium (Ca_t) concentrations are significantly higher (p-value < 0.05) in the Upper and Lower Ice Complexes (UIC and LIC; 5.1 ± 2.1 g/kg) and in the Lower Sand Unit (5.9 ± 1.6 g/kg) than in the younger units (OL and HC; 2.7 ± 0.6 g/kg, Figure 3a). For the concentrations in major elements such as iron (Fe) and aluminum (Al), there is no significant difference between Holocene Cover and Woody Debris and units deposited during glacial periods (LIC, LSU, and UIC), that is, 27 ± 3 g/kg for Fe and 62 ± 4 g/kg for Al (Figure 3b,c).

3.2 | Selective Mineral Elements and Organic Carbon Extractions

Within all profiles, Fe is the dominant metal involved in complexes ($Fe_p/(Fe_p + Al_p + Mn_p) = 50 \pm 11\%$ on a molar basis: mmol/kg), followed by Al ($Al_p/(Fe_p + Al_p + Mn_p) = 39 \pm 7\%$) and Mn ($Mn_p/(Fe_p + Al_p + Mn_p) = 11 \pm 6\%$) (see also Figure S5). The proportion of Fe bound to OC in the form of complexes relative to total Fe (Fe_p/Fe_t) is 3 ± 4%. This proportion of Fe in the form of complexes is not uniform within the stratigraphic units: The surface organic layer sample reaches 21%, followed by the Woody Debris layer (6 ± 3%), the Holocene Cover (4 ± 1%), the Upper Ice Complex (3 ± 3%), and, finally, the Lower Ice Complex (1.2 ± 0.5%) and the Lower Sand Unit (0.7 ± 0.3%).

For Al, the proportion of complexes relative to the total Al is overall much lower than for Fe ($Al_p/Al_t = 0.5 \pm 0.7\%$) and is highest in the shallow organic sample (OL; 4.6%) followed by the Woody Debris layer (0.7 ± 0.3%), the Holocene Cover, and the Upper Ice Complex (HC and UIC; 0.5 ± 0.4%) and the deepest units (LSU and LIC; 0.17 ± 0.04%). For Mn, the proportion of complexes relative to the total Mn (Mn_p/Mn_t) is higher (30 ± 13%) than for Fe and Al and is the highest within the organic layer sample (60%), the lowest within the Holocene Cover samples (9 ± 4%) and relatively constant within the other units (UIC, WD, LSU, LIC; 31 ± 12%).

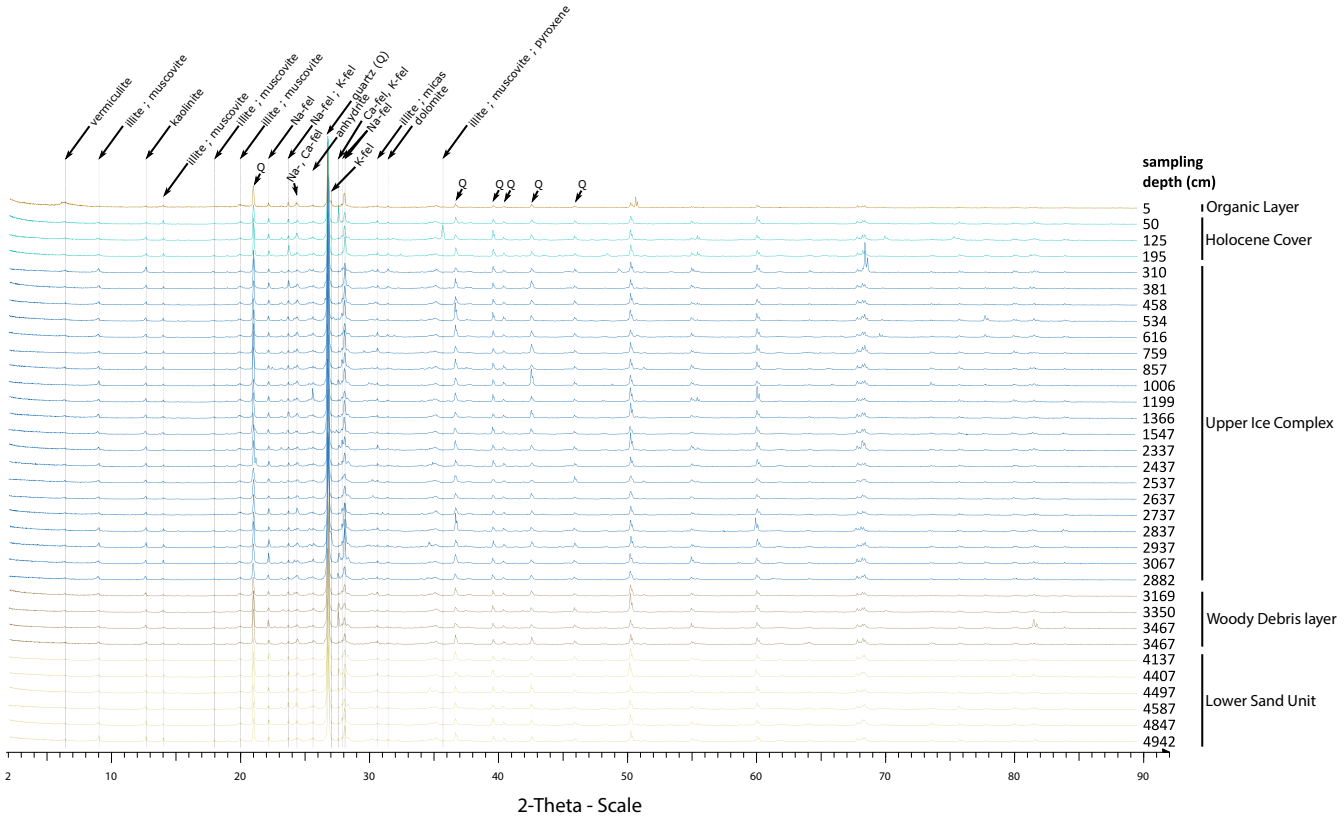

FIGURE 2 | Diffractograms for Batagay thaw slump in sediment profile 1. Colors represent the stratigraphic units, namely, from the top to the bottom: the organic layer (OL, $n = 1$, light brown), Holocene Cover (HC, $n = 3$, light blue), Upper Ice Complex (UIC, $n = 20$, dark blue), Woody Debris layer (WD, $n = 4$, dark brown), and Lower Sand Unit (LSU, $n = 6$, yellow). Q = quartz, fel = feldspar (K–, Na– and Ca–).

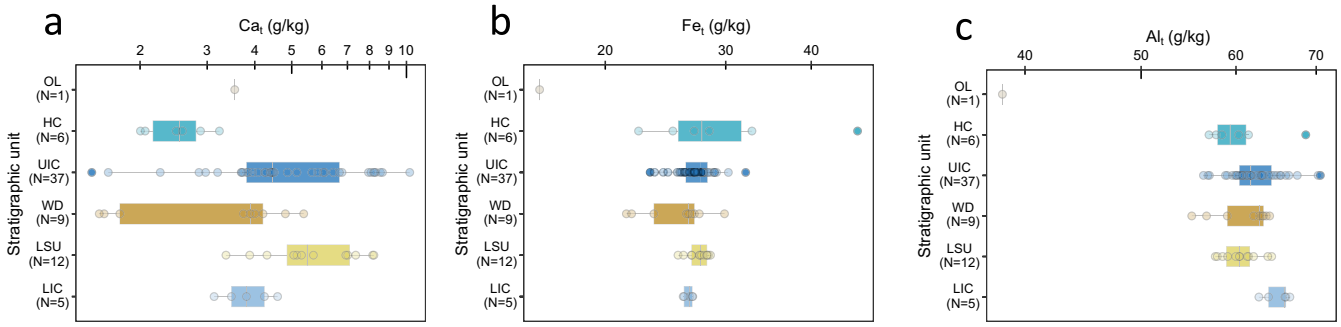

FIGURE 3 | Boxplots of (a) total calcium (Ca_t), (b) total iron (Fe_t), and (c) total aluminum (Al_t) concentrations within the stratigraphic units of the Batagay thaw slump, namely, from the top to the bottom: the organic layer (OL), Holocene Cover (HC), Upper Ice Complex (UIC), Woody Debris layer (WD), Lower Sand Unit (LSU), and Lower Ice Complex (LIC). Concentrations are given in grams of element per kilogram of dry matter.

Overall, the sum of metal complexes ($Fe_p + Al_p + Mn_p$ in mmol/kg) is the highest in the organic layer, followed by the Woody Debris layer, in which this sum is significantly higher than in the Holocene Cover and the Upper Ice Complex (p-value < 0.05), in which the sum is significantly higher than in the Lower Sand Unit and the Lower Ice Complex (Figure S5). When considering the metals most dominant to form complexes with OC individually, Fe is found to explain most of the variability in the C_p distribution (robust linear regression plot between C_p and Fe_p; R^2 adj = 0.82; Figure S6a), followed by Al_p (R^2 adj = 0.76; Figure S6b) and Mn_p (R^2 adj = 0.49; Figure S6c). Still, these three metals together provide a better explanation of the distribution of C_p concentrations (R^2 adj = 0.84; Figure S6d).

The proportion of reactive Fe (Fe_o/Fe_t, i.e., the ratio between the oxalate-extracted Fe concentration and the total Fe concentration) reaches overall 12 ± 8%. It decreases with increasing age of the stratigraphic units (Figure 4a): It drops from 33 ± 12% in the organic layer and Holocene Cover samples to 7 ± 2% in the oldest glacial deposit (LIC). The proportion of Fe as poorly crystalline oxides (i.e., $(Fe_o - Fe_p)/Fe_t$) also decreases (p-value < 0.05) with increasing age of the deposit, from 28 ± 14% for Holocene deposits to 6 ± 2% for Middle Pleistocene deposits (LIC).

Total organic carbon (TOC) content varies within the Batagay headwall but remains low at 1.2 ± 0.6%, except in the organic layer (OL) where it reaches 15% (Figure 4b). With increasing depth, the TOC content reaches a maximum within the Woody Debris layer (1.7 ± 0.5%) and then decreases for the lower ice complex (LIC; 0.7 ± 0.1%). The proportion of TOC forming complexes with metals (C_p/TOC) follows the same general pattern as for the TOC content and represents 29 ± 8% of the TOC pool but with smaller variations between units (Figure 4c). Assuming a maximum sorption capacity of 0.22 g_{OC}/g_{Fe} [81], we can estimate a maximum proportion of 5 ± 4% of TOC bound to poorly crystalline Fe oxides ($Fe_o - Fe_p$) within the Batagay headwall. This proportion is highest for the Holocene Cover (19 ± 6%) and remains significantly lower for all other units (OL; UIC; WD; LSU; LIC; 4 ± 2%). Lastly, the optical density of oxalate extract (ODOE) is highest for the organic layer (0.365), has the lowest values for the Lower Sand Unit (0.02 ± 0.01), and is intermediate, but more variable, for the other units (HC; UIC; WD; LIC; 0.08 ± 0.05; Table S1).

4 | Discussion

4.1 | Batagay Stratigraphic Units: Similar Geological Nature but Different Historical Permafrost Thaw Dynamics

The similar mineral phases found within the different stratigraphic units of the Batagay headwall (Figures 2, S3, and S4) suggest that the geological nature of the source of the sediments did not vary significantly along the depositional period ranging from ~650 ka to modern, which is consistent with the formation of deposits involving ice-rich Yedoma [82–84]. The lower Ca_t concentrations in the Holocene Cover and the Woody Debris layers compared to the glacial deposits (LIC, LSU, and UIC) (Figure 3a) suggest, however, that the conditions for the leaching of more soluble elements such as Ca has not been homogeneous within the period of deposition. The lower Ca_t concentrations likely reflect conditions for a higher leaching of solutes during warmer and/or wetter periods (i.e., HC and WD units). The Woody Debris layer is interpreted as a forest bed supposed to be of last interglacial (MIS 5e) age. It therefore likely experienced warm climate stages [85, 86], with favorable conditions for pedological development. The near-surface Holocene Cover is also characterized by soil formation processes [64] and wet depositional conditions are furthermore confirmed by biomarker data [20]. By contrast, drier depositional conditions especially during the coldest periods are reflected by isotopic and paleo-ecological analyses in the units representative of the glacial periods (LIC, LSU, and UIC) [87, 88]. This is confirmed by minor variations in the biogeochemical and biomarker parameters for the same units [20]. From this, it can be inferred that the deposits of the different stratigraphic units of the Batagay thaw slump have a similar source but contrasted conditions of sedimentation, freezing and historical permafrost thaw dynamics.

4.2 | Mineral-Bound Organic Carbon in the Batagay Megaslump Dominated by Complexation With Metals

Our data demonstrate that the proportion of mineral-bound OC within the headwall of the Batagay megaslump is dominated by the complexation with metals (29 ± 8% of the TOC; Figure 4c) compared to TOC bound to poorly crystalline Fe

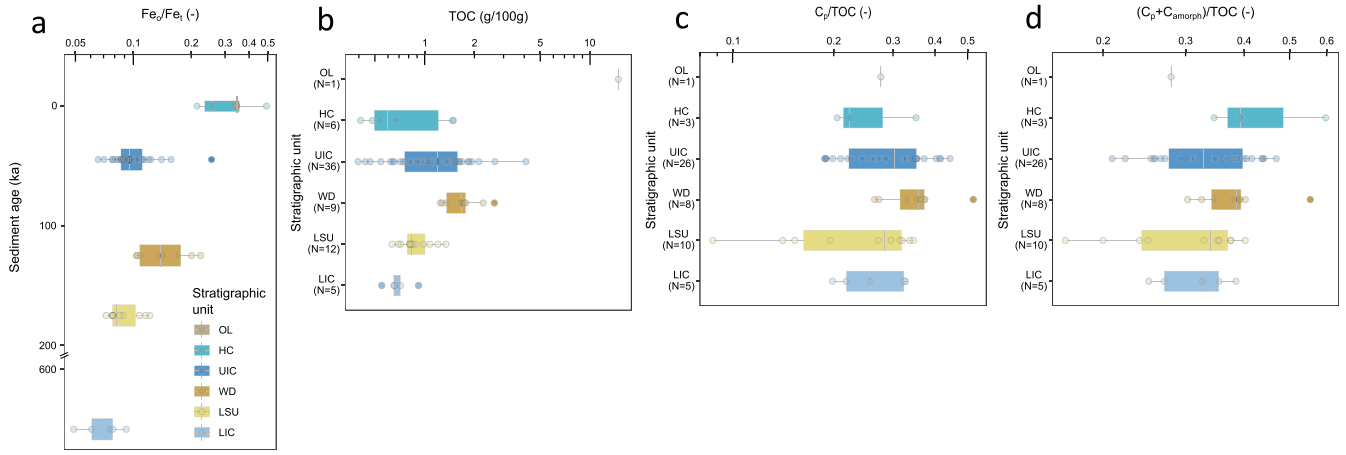

FIGURE 4 | Boxplots of (a) the ratio oxalate-extracted iron with regard to total iron (Fe_o/Fe_t) as a function of the Batagay sediments depositional age. This Fe either form organo-metallic complexes or associations with OC; (b–d) evolution within the stratigraphic units of the Batagay thaw slump of (b) total organic carbon (TOC) in sediments and (c) pyrophosphate-extracted carbon in regard to total organic carbon (C_p/TOC) in sediments. This refers to the proportion of OC forming complexes with metals; (d) sum of proportions of pyrophosphate-extracted carbon and maximum proportion of OC bound to poorly crystalline Fe oxides (($C_p + C_{amorph}$)/TOC) in sediments. This refers to OC that interacts with minerals via complexation with metals or associations to poorly crystalline iron oxides. The stratigraphic units of the Batagay thaw slump are, from the top to the bottom, the organic layer (OL), Holocene Cover (HC), Upper Ice Complex (UIC), Woody Debris layer (WD), Lower Sand Unit (LSU), and Lower Ice Complex (LIC). The values of C_{amorph} correspond to a maximum sorption capacity of OC to poorly crystalline Fe oxides (0.22 g_{OC}/g_{Fe} as ferrihydrite). Sediment depositional age as in Table 1. TOC content is given in grams of OC per 100 g of dry matter (wt, %).

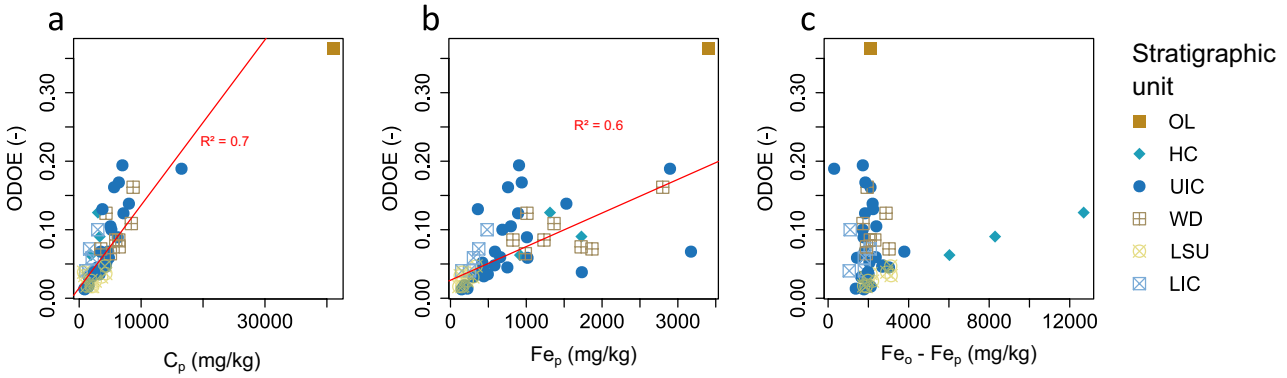

FIGURE 5 | Robust linear regression plot between optical density of oxalate extract (ODOE) and (a) pyrophosphate-extracted carbon (C_p), (b) pyrophosphate-extracted iron (Fe_p), and (c) difference between oxalate-extracted iron and pyrophosphate-extracted iron ($Fe_o - Fe_p$). HC = Holocene Cover, LIC = Lower Ice Complex; LSU = Lower Sand Unit; OL = organic layer, UIC = Upper Ice Complex, WD = Woody Debris layer.

oxides (5 ± 4%), with an exception for the Holocene Cover, which has a substantial maximal sorption capacity of OC to amorphous Fe oxides (Figure 4c,d). Besides, our measurements of the optical density of oxalate extract (ODOE), representing organic acids forming complexes and adsorbed onto poorly crystalline minerals, show a correlation with the concentration in OC forming complexes with metals (C_p; R^2 adj = 0.7; Figure 5a), as well as with the Fe involved in these complexes (Fe_p, Figure 5b), but no correlation with the Fe in the form of poorly crystalline Fe oxides (Fe_o-Fe_p, Figure 5c) except for the Holocene Cover. This supports that complexation is the dominant mechanism for OC–mineral interactions in the sediments involved in the Batagay thaw slump, except in the Holocene Cover. Totaling the contributions of OC forming complexes with metals (C_p/TOC) and the maximum sorption capacity of OC to poorly crystalline Fe oxides (C_{amorph}/TOC), this results in a maximal total proportion of 34 ± 8% of the TOC that interacts with either mineral surfaces or mineral elements (Figures 4 and S7), with a maximum value for the Holocene Cover (45 ± 13%) and a minimum value for the Lower Ice Complex (32 ± 6%).

Apart from the Woody Debris layer, the proportion of OC forming complexes with metals (C_p/TOC) does not vary significantly between stratigraphic units (Figure 4c), even though the TOC content differs between units as a function of the environmental conditions at the time of deposition (Figure 4b). This is supported by Jongejans et al. [20] and references therein. Moreover, the concentration of OC forming complexes with metals (C_p) is proportional to the TOC content (R^2 adj = 0.9; see also Supporting Information S5). This suggests that alternating glacial (with the deposition of LIC, LSU & UIC) and interglacial periods (with the deposition of HC and WD) controls C_p and TOC content to some extent but

does not fully control the ratio of OC that forms complexes with metals (C_p/TOC). The homogeneity of the proportion C_p/TOC within the entire Batagay headwall suggests that metal–organic complexes seem to be stable over time across multiple glacial and interglacial periods. In contrast, OC associations to poorly crystalline Fe oxides seem to be proportionally more limited, and driven by warmer and wetter conditions with the deposition of the Holocene Cover [20, 85].

4.3 | Interglacial Period Deposits: Mineral–OC Interactions and Intrinsic Chemical Composition of OC

From Sections 3.2 and 4.2, we note that the Holocene Cover shows the highest proportion of OC–mineral interactions (($C_p + C_{amorph}$)/TOC; Figure 4d) and that the Woody Debris layer shows the highest concentration of OC forming complexes with metals (C_p), without considering the surface organic layer (see also Table S1). Biomarker data from samples collected from the same depths [20] indicate that the Holocene Cover shows a higher level of degradation and thus a lower quality for organic matter, which makes it therefore less likely to be degraded in the future. Furthermore, high microbial decomposition (favored by higher soil temperatures) within the Woody Debris layer is confirmed by higher-plants fatty acid (HPFA) indexes [20]. This increased level of microbial transformation of OC and consequent lower quality of organic matter, suggests that further degradation is also unlikely to occur in the future. In contrast, the stratigraphic units corresponding to glacial periods (UIC, LSU, and LIC) probably experienced lower microbial activity than the other stratigraphic units [20]. Consequently, biogeochemical legacy of interglacial periods reveal that the organic matter contained in such units has undergone greater microbial transformation [20] and contain a greater proportion of mineral-bound OC. Increased microbiological activity at the time of deposition, combined with warm climate stages and favorable conditions for pedological development turn out to be key factors leading to an OC less likely to contribute to the permafrost-carbon-climate feedback.

4.4 | Forms of Mineral–OC Interactions: Comparison Across Different Permafrost Sites

In order to position the Batagay sediments within other Arctic regions in terms of organo-mineral interactions, we compared the data from this study with available data from other locations (Figures 6 and 7). It turns out that the pool of mineral-interacting forms of OC in Batagay are comparable to what is found in other thermokarst landforms. More specifically, the comprehensive mineral-interacting proportion of TOC (i.e., via associations with poorly crystalline Fe oxides and in complexed form; ($C_p + C_{amorph}$)/TOC) from Batagay is (i) in line with the literature for both drained thaw lake basins in northern Alaska [54] and slump deformations in the Qinghai-Tibetan Plateau [43], as for Peel Plateau (Canada) thaw slumps [46], circum-Arctic Yedoma sediments [92] and lowland thermokarst landscape in Eight Mile Lake, Alaska [95], (ii) higher than in palsa [94] and in marine

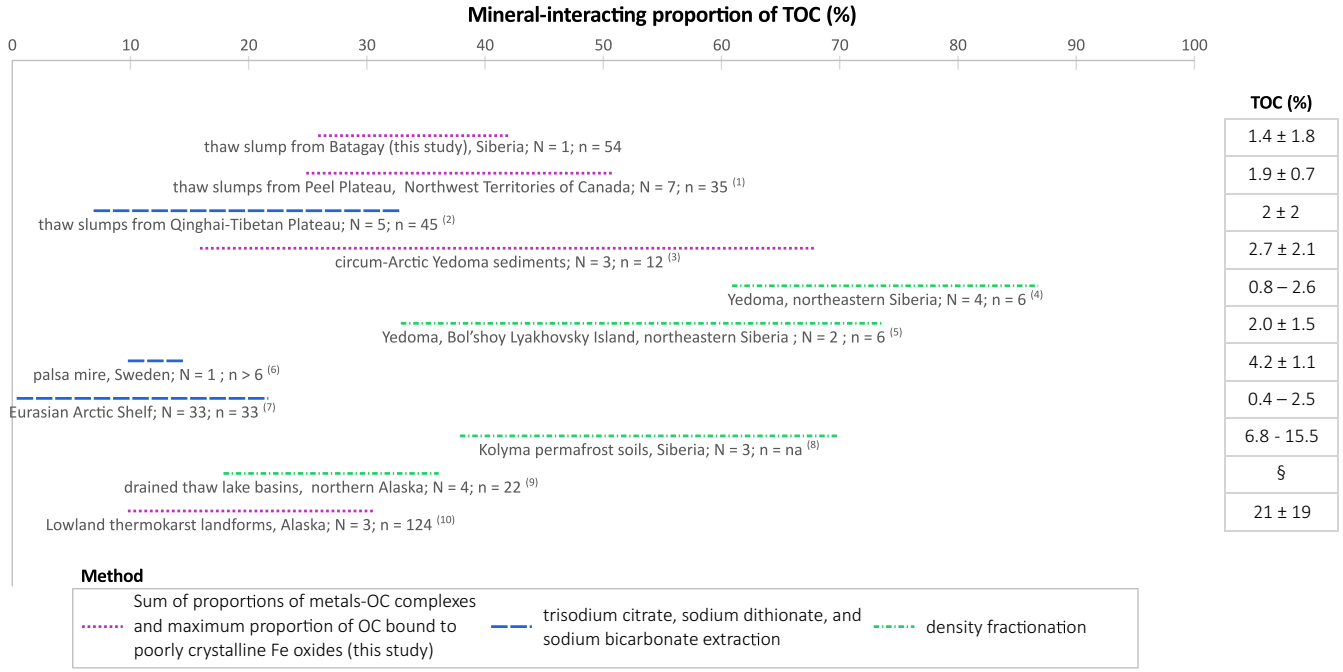

FIGURE 6 | Comparison of mineral-interacting forms of OC in the entire headwall of the Batagay thaw slump, with other contrasting deposits throughout the Arctic. The percentages are given on a mass basis. Three different methods have been used: the sum of proportions of metals–OC complexes and maximum proportion of OC bound to poorly crystalline Fe oxides as in this study (purple); trisodium citrate, sodium dithionate, and sodium bicarbonate extraction from Lalonde et al. [51], Mehra and Jackson [89], and Poulton and Canfield [90] (blue) and density fractionation method with sodium polytungstate in Dutta et al. [53], Gentsch et al. [91], and Mueller et al. [54] (green). §OC expressed in stock: 54 ± 15 kg/m^{-3}. *N* = number of sites/cores; *n* = number of samples. na = not available. (1)Thomas et al. [46]; (2)Mu et al. [43]; (3)Monhonval et al. [92]; (4)Dutta et al. [53]; (5)Martens et al. [93]; (6)Patzner et al. [94]; (7)Salvadó et al. [55]; (8)Gentsch et al. [91]; (9)Mueller et al. [54]; (10)Monhonval et al. [95].

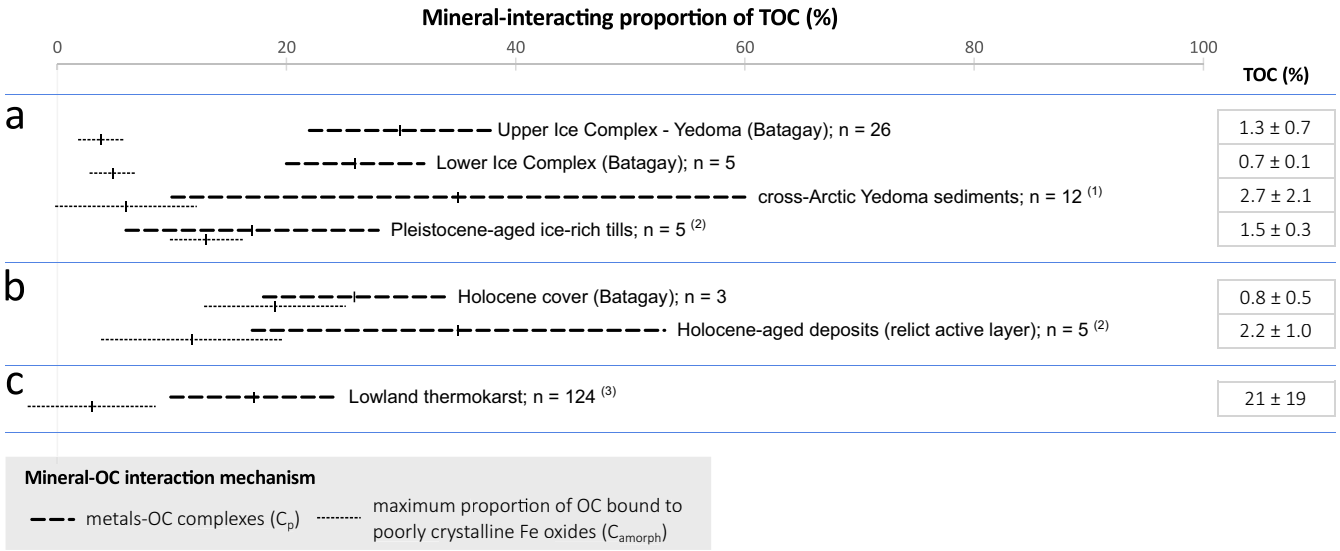

FIGURE 7 | Comparison of mineral-interacting forms of OC in the Upper Ice Complex (UIC), Lower Ice Complex (LIC), and Holocene Cover (HC) units within the Batagay thaw slump, with other similar deposits throughout the Arctic. (a) Ice-rich sediments; (b) sediments from interglacial periods; (c) sediments from lowland thermokarst landforms. We used the maximum sorption capacity of OC to poorly crystalline Fe oxides (0.22 g_{OC}/g_{Fe} as ferrihydrite). The percentages are given on a mass basis. The distributions are represented by the mean ± standard deviation. (1)Circum-Arctic Yedoma sediments [92]; (2)layers from thaw slump headwalls from the Peel Plateau, Western Canadian Arctic [46]; (3)Eight Mile Lake, Central Alaska [95].

sediments from the Eurasian Arctic Shelf [55], and (iii) in the low range compared to Yedoma from the Bol'shoy Lyakhovsky Island [93] and soils from the Lower Kolyma Region ([91]; Figure 6; Table S2) and significantly lower than Yedoma permafrost in northeastern Siberia [53]. The active layer (and generally the surface organic layers) appear to have a lower proportion of mineral-interacting OC than in the less TOC-rich permafrost layers [91, 95]. This could be attributed to a relative OC oversaturation in regard the mineral surfaces or elements available for mineral–OC interactions in the superficial layers and possible inputs of modern labile OC from actively growing plants. This is also observed in palsa (sampling depths < 25 cm in [94]) and in superficial sediment samples from the Eurasian Arctic Shelf [55]. The proportions of mineral-bound OC in Yedoma sediments [53, 92, 93] are highly variable between sites. It can be argued that this results from the polygenetic origin of Yedoma deposits, with seasonally differentiated deposition mechanisms controlled by local environmental conditions, including the contribution from local fluvial, colluvial, and alluvial sediments [77, 96, 97].

Beyond the numerical results, we acknowledge that the method for obtaining a comprehensive assessment of mineral-interacting proportion of TOC does not appear to be a critical factor. More specifically, the method used in this study, or the trisodium citrate, sodium dithionate, and sodium bicarbonate extraction method [51, 89, 90] or even the density fractionation method with sodium polytungstate, does not appear to give results that are systematically biased in either direction (Figure 6).

Where possible, we compared the mechanisms involved in OC–mineral interactions, i.e., complexation or associations with poorly crystalline Fe oxides. In ice-rich sediments (Figure 7a), the proportions of OC forming complexes with metals are comparable, but the potential for association with poorly crystalline Fe oxides is more variable. More specifically, pyrophosphate-extracted carbon (C_p) concentrations are in the same range between (i) the two ice complex units in Batagay (UIC—or Yedoma—and LIC), (ii) circum-Arctic Yedoma sediments [92], (iii) undisturbed Yedoma in Yukechi [98], and (iv) Pleistocene-aged ice-rich tills in the Peel Plateau [46], even though there is more variability in the Yedoma at the Arctic scale (Table S3). The proportion of OC in the form of complexes with metals (C_p/TOC; Figure 7a; Table S3) is also similar for the different studies. The maximum sorption capacity of the OC to poorly crystalline Fe oxides (C_{amorph}/TOC), on the other hand, shows more variability between sites, with higher values within the Pleistocene-aged ice-rich tills in the Peel Plateau compared to the Lower Ice Complex and Upper Ice Complex (Yedoma) deposits in Batagay. This also applies for reactive Fe (Fe_o) concentrations and the proportion of reactive Fe to total Fe (Fe_o/Fe_t) (Table S3).

We also compared sediments from interglacial periods with other locations (Figure 7b). This supports the argument that wet depositional conditions, warm climate stages and pedological development appear to be key conditions for a highest potential for OC association with poorly crystalline Fe oxides. Furthermore, this seems to be applicable beyond a single site. Specifically, that maximal proportion of OC sorbed to poorly crystalline Fe oxides (C_{amorph}/TOC) is significantly higher in the Batagay Holocene Cover (HC) than in (i) all other units of the Batagay thaw slump headwall; (ii) circum-Arctic Yedoma sediments [92] and (iii) permafrost soils in lowland thermokarst landforms [95] (Figure 7a). The Holocene Cover at Batagay is otherwise comparable with Holocene-modified deposits in the Peel Plateau that experienced past thaw during the Holocene thermal maximum ([46]; Figure 7b), while falling within the upper range compared to Pleistocene-aged ice-rich tills in the Peel Plateau (Figure 7a).

When comparing the Batagay thaw slump (entire headwall; Figure 7a,b) with lowland thermokarst landforms ([95]; Figure 7c), the pyrophosphate-extracted carbon (C_p) and TOC content at Batagay are in the low range of values found in region

of lowland thermokarst degradation, but the complexed fraction relative to the total (C_p/TOC) is in the same range (Table S2). Overall, this suggests that OC–metal complexation is the dominant mechanism within the mineral-interacting forms of OC, regardless of the sampling location.

4.5 | Interglacial Period Deposits: Only 25% of the OC Mass Mobilized From the Sediments of the Batagay Thaw Slump

Using the sampling depths along the headwall and an estimate of the headwall retreat rate [35], we established a first-order estimate of ~10^6 m^3 of total volume retreated annually from the Batagay collapse front (on average, between 1991 and 2018). This volume estimate is in line with Günther et al. [30] who derived a total thawed volume of 2.4×10^7 m^3 through 2014, that is, ~0.7×10^6 m^3/year, assuming that the second stage of the disturbance (i.e., causing rapid thermo-denudational development of the thaw slump; [64]) started at the end of the 1980s. Using the bulk density of the sediments and TOC content on the profile, we were able to establish an estimate of ~1.2×10^7 kg of OC mobilized annually from the Batagay thaw slump (Figure 8a). Beyond the absolute value of this mobilized mass, this reveals that the units deposited during the glacial periods (i.e., UIC, LSU, and LIC), together represent 72% of the OC mass mobilized from the Batagay thaw slump. We note that deposits from interglacial periods account jointly ~25% of the OC mobilized from the slump, even though they resulted in a greater proportion of the mineral-bound OC pool. In relative terms, the units that show the greater portion of OC within the Batagay slump headwall therefore do not contribute much to the total mass of OC mobilized by the collapsing feature.

The OC flux estimate is subject to significant uncertainties. First, it was not possible to consider the Upper Sand Unit in the calculation, as it was not sampled in this study. After estimation based on Kizyakov et al. [63] the Upper Sand Unit, however, only represents a vertical surface area of about 2% of the headwall (based on the structure of the western part of the RTS vertical headwall). We acknowledge that more downslope and across all former headwalls, the Upper Sand Unit could potentially represent about 15 m in thickness [88]. Additionally, the stratigraphic units do not have a uniform thickness along the headwall. For instance, the exposed thickness of the Lower Sand Unit decreases to ~zero in the northwestern part of the central headwall (while the thickness of the Upper Ice Complex increases). Yet, it can be seen within Kizyakov et al. [63] that, overall, the stratigraphic units that have the largest mass balance contribution (UIC and LSU) have thicknesses that do not vary for more than 4 m for the UIC and 8 m for the LSU (based on 2019 field observation within observed headwalls). For the UIC, an additional 4 m thick contribution represents a potential increase in the volume estimate of 0.1×10^6 m^3/year and

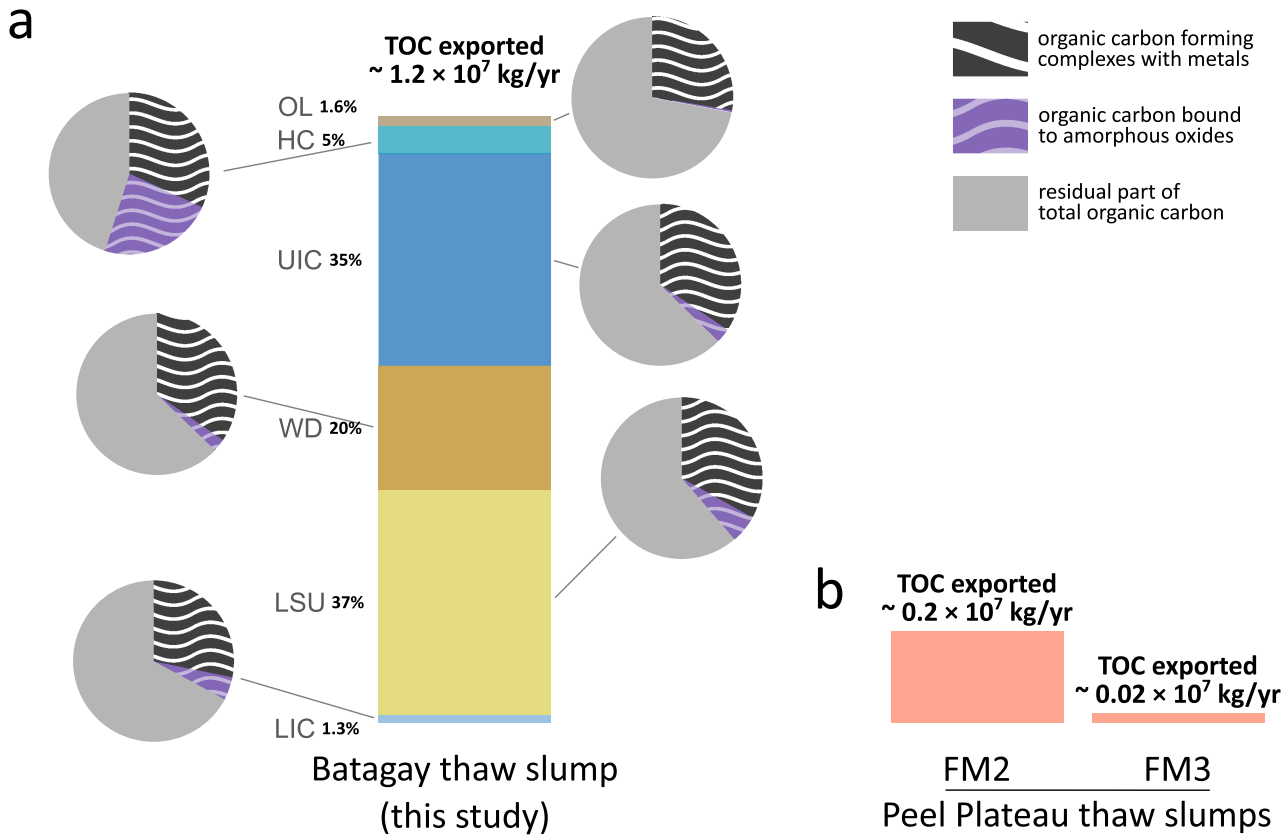

FIGURE 8 | Annual mass balance assessment of the sediment material eroded by the retreat of the collapse front of the Batagay thaw slump in comparison to Peel Plateau thaw slumps. (a) Batagay thaw slump displaced material mass distribution modeling within the different stratigraphic units (bar-plot) and mass proportion of mineral-interacting forms of organic carbon within the units (pie-charts). HC = Holocene Cover, LIC = Lower Ice Complex (LIC), LSU = Lower Sand Unit; OL = organic layer, UIC = Upper Ice Complex, and WD = Woody Debris layer with color codes following Figures 2–5. (b) Comparison with Peel Plateau thaw slumps FM2 and FM3 (data from [46]). TOC = total organic carbon.

~0.01×10^7 kg/year (1%) increase in TOC mobilization, based on the *average* TOC content for this unit. Similarly, 8-m-thicker LSU for the entire headwall would represent an increase in 3% of TOC mobilization. Finally, headwall height is not uniform throughout the collapse front. All these considerations imply that the flux estimate presented in this study should be considered as a first order estimate, which is not intended to be more accurate than within an order of magnitude. Another point to note is that this mass balance does not take into account the dissolved organic carbon (DOC) that may be present in ice wedges. According to Fritz et al. [99], who analyzed different ice bodies throughout the Arctic, ice wedges could contain up to 28.6 mg/L of DOC. For the Batagay slump, Kizyakov et al. [100] found a mean ice wedge DOC content of 19 mg/L as a first estimate based on 47 samples. If we extrapolate this concentration to the entire volume of ice exported by the Batagay megaslump annually, we obtain a first order estimate of 10^4 kg of DOC per year, which is three orders of magnitude lower than the mass of TOC exported by the sediments. If we consider comparatively higher concentrations of DOC for the pore ice in the sediments, that is, a mean of to 560 mg/L [100] and carry out the same extrapolation procedure, we obtain 3×10^5 kg DOC per year exported by the ice, which corresponds to 2% of the OC exported by the sediments. Even so, we recognize that DOC, although not representing a substantial part of the mass balance, is still of major importance for biogeochemical processes, being potentially highly labile compared to sediment TOC [11, 12, 101]. When comparing the mass of OC mobilized by the Batagay thaw slump to the masses mobilized by megaslumps from the Peel Plateau in Canada [46] (FM2 headwall height = 18.6 m and scar zone area = 32.7 ha; FM3 headwall height = 6.5 m and scar zone area = 6.7 ha; 46] and references therein), it appears that the mass of OC mobilized by the Batagay thaw slump is ~7 times greater than that mobilized by that of the slump FM2 and ~65 times greater than that mobilized by slump FM3 (Figure 8b). Yet, slump FM3 at the Peel Plateau is already qualified as a mega-slump and still mobilizes ~65 times less OC than Batagay. We note that a portion of the debris mobilized by the Batagay thaw slump can potentially refreeze after headwall erosion and burial in the slumped zone, resulting in permafrost re-establishment in the scar zone as the slump stabilizes [102, 103]. In Batagay, however, there is a clear predominance of the erosion process (removal of material and deepening of the channel), which is evidenced by a narrow erosional valley with a V-shaped transverse profile. Yet, it is not expected that all of the debris would be effectively exposed to thaw after slump-induced mobilization of material. Further studies are needed to quantify the full image of C flux, including losses as gas and the particulate proportion that stabilizes locally and refreezes, out of which a portion forms a new active-layer within the scar zone.

5 | Conclusions

We studied the mechanism for OC–mineral interactions within the Batagay megaslump, the largest known thaw slump headwall exposing the second oldest directly dated permafrost in the Northern Hemisphere. We compared our results with available data from other locations in the Arctic and established a first order estimate of the mass of material eroded annually by the retreat of the collapse front, along with an overall assessment of the OC–mineral interactions within this mobilized material. In conclusion, we found that:

(i) Deposits of the Batagay stratigraphic units have a similar geological nature but different historical permafrost thaw dynamics.

(ii) Within the Batagay headwall, complexation is the dominant mechanism for OC–mineral interactions in the sediments and represents 29 ± 8% of the TOC, while we estimate a maximal proportion of 5 ± 4% of the TOC involved in OC-Fe oxide associations. We estimate accordingly that the combination of the two mechanisms results in 34 ± 8% of the TOC pool that interacts with mineral surfaces or elements.

(iii) The forms and proportion of OC–mineral interactions at Batagay are in the same range quantitatively, compared to those found in other hillslope thermokarst landforms.

(iv) Batagay sediments from interglacial periods show higher OC–mineral interactions, along with organic matter that has undergone more microbial transformation and is therefore presumably less biodegradable. Yet, such units account jointly for ~25% of the OC mass mobilized from the Batagay thaw slump.

(v) We provide a first order estimate of ~1.2×10^7 kg of OC mobilized annually downslope of the headwall, with a maximum of 38% interacting with mineral element or surfaces by complexation with metals or associations to poorly crystalline iron oxides.

These data support that more than one-third of the TOC exposed by this massive thaw slump is not directly available for mineralization but rather interacting with the mineral fraction of the sediments.

Acknowledgments

The authors acknowledge fieldwork support from Dmitry Ukhin, Hanno Meyer, Jeremy Courtin, Igor Syromyatnikov, and Andrei Shepelev. The authors further acknowledge Laurence Monin, Claudine Givron, Élodie Devos, and Hélène Dailly from the Mineral and Organic Chemical Analysis (MOCA) platform at UCLouvain for conducting chemical analysis and Arthur Monhonval, Catherine Hirst, and all the members of the WeThaw project for useful discussions. M.T. thanks the members of the ELIE-SOIL lab for useful critical comments.

Conflicts of Interest

The authors declare no conflicts of interest.

Data Availability Statement

All data are made available as supporting information to the paper.

References

1. M. Rantanen, A. Y. Karpechko, A. Lipponen, et al., "The Arctic Has Warmed Nearly Four Times Faster Than the Globe since 1979," *Communications Earth & Environment* 3 (2022): 1–10, https://doi.org/10.1038/s43247-022-00498-3.

2. S. Dobricic and L. Pozzoli, *Arctic Permafrost Thawing: Impacts on High Latitude Emissions of Carbon Dioxide and Methane* (LU: Publications Office of the European Union, Luxembourg, 2019), https://doi.org/10.2760/007066.

3. IPCC, *IPCC Special Report on the Ocean and Cryosphere in a Changing Climate: Summary for Policymakers*, eds. H.-O. Pörtner, D. C. Roberts, V. Masson-Delmotte, et al. (Cambridge, UK and New York, NY, USA: Cambridge University Press, 2019), 3–35, https://doi.org/10.1017/9781009157964.001.

4. M. R. Turetsky, B. W. Abbott, M. C. Jones, et al., "Permafrost Collapse Is Accelerating Carbon Release," *Nature* 569 (2019): 32–34, https://doi.org/10.1038/d41586-019-01313-4.

5. B. W. Abbott and J. B. Jones, "Permafrost Collapse Alters Soil Carbon Stocks, Respiration, CH_4, and N_2O in Upland Tundra," *Global Change Biology* 21 (2015): 4570–4587, https://doi.org/10.1111/gcb.13069.

6. C. D. Koven, B. Ringeval, P. Friedlingstein, et al., "Permafrost Carbon-Climate Feedbacks Accelerate Global Warming," *PNAS* 108 (2011): 14769–14774, https://doi.org/10.1073/pnas.1103910108.

7. D. M. Lawrence, C. D. Koven, S. C. Swenson, W. J. Riley, and A. G. Slater, "Permafrost Thaw and Resulting Soil Moisture Changes Regulate Projected High-Latitude CO_2 and CH_4 Emissions," *Environmental Research Letters* 10 (2015): 094011, https://doi.org/10.1088/1748-9326/10/9/094011.

8. A. D. McGuire, D. M. Lawrence, C. Koven, et al., "Dependence of the Evolution of Carbon Dynamics in the Northern Permafrost Region on the Trajectory of Climate Change," *PNAS* 115 (2018): 3882–3887, https://doi.org/10.1073/pnas.1719903115.

9. E. Schuur, A. D. McGuire, C. Schädel, et al., "Climate Change and the Permafrost Carbon Feedback," *Nature* 520 (2015): 171–179, https://doi.org/10.1038/nature14338.

10. M. R. Turetsky, B. W. Abbott, M. C. Jones, et al., "Carbon Release Through Abrupt Permafrost Thaw," *Nature Geoscience* 13 (2020): 138–143, https://doi.org/10.1038/s41561-019-0526-0.

11. J. E. Vonk, P. J. Mann, S. Davydov, et al., "High Biolability of Ancient Permafrost Carbon Upon Thaw," *Geophysical Research Letters* 40 (2013a): 2689–2693, https://doi.org/10.1002/grl.50348.

12. J. E. Vonk, L. Sánchez-García, B. E. van Dongen, et al., "Activation of Old Carbon by Erosion of Coastal and Subsea Permafrost in Arctic Siberia," *Nature* 489 (2012): 137–140, https://doi.org/10.1038/nature11392.

13. G. Hugelius, J. Strauss, S. Zubrzycki, et al., "Estimated Stocks of Circumpolar Permafrost Carbon With Quantified Uncertainty Ranges and Identified Data Gaps," *Biogeosciences* 11 (2014): 6573–6593, https://doi.org/10.5194/bg-11-6573-2014.

14. J. Strauss, B. W. Abbott, G. Hugelius, et al., "Permafrost," in *Recarbonizing Global Soils—A Technical Manual of Recommended Management Practices*, (Rome, Italy: FAO, 2021a), https://doi.org/10.4060/cb6378en.

15. C. Plaza, E. Pegoraro, R. Bracho, et al., "Direct Observation of Permafrost Degradation and Rapid Soil Carbon Loss in Tundra," *Nature Geoscience* 12 (2019): 627–631, https://doi.org/10.1038/s41561-019-0387-6.

16. M. S. Patzner, M. Logan, A. M. McKenna, et al., "Microbial Iron Cycling During Palsa Hillslope Collapse Promotes Greenhouse Gas Emissions Before Complete Permafrost Thaw," *Communications Earth & Environment* 3 (2022): 1–14, https://doi.org/10.1038/s43247-022-00407-8.

17. C. Schädel, M. K.-F. Bader, E. A. G. Schuur, et al., "Potential Carbon Emissions Dominated by Carbon Dioxide From Thawed Permafrost Soils," *Nature Climate Change* 6 (2016): 950–953, https://doi.org/10.1038/nclimate3054.

18. J. E. Vonk, S. E. Tank, and M. A. Walvoord, "Integrating Hydrology and Biogeochemistry Across Frozen Landscapes," *Nature Communications* 10 (2019): 5377, https://doi.org/10.1038/s41467-019-13361-5.

19. L. Bröder, C. Hirst, S. Opfergelt, et al., "Contrasting Export of Particulate Organic Carbon From Greenlandic Glacial and Nonglacial Streams," *Geophysical Research Letters* 49 (2022): e2022GL101210, https://doi.org/10.1029/2022GL101210.

20. L. L. Jongejans, K. Mangelsdorf, C. Karger, et al., "Molecular Biomarkers in Batagay Megaslump Permafrost Deposits Reveal Clear Differences in Organic Matter Preservation Between Glacial and Interglacial Periods," *The Cryosphere* 16 (2022a): 3601–3617, https://doi.org/10.5194/tc-16-3601-2022.

21. S. Opfergelt, "The Next Generation of Climate Model Should Account for the Evolution of Mineral-Organic Interactions With Permafrost Thaw," *Environmental Research Letters* 15 (2020): 091003, https://doi.org/10.1088/1748-9326/ab9a6d.

22. S. M. Natali, J. P. Holdren, B. M. Rogers, et al., "Permafrost Carbon Feedbacks Threaten Global Climate Goals," *Proceedings of the National Academy of Sciences* 118 (2021): e2100163118, https://doi.org/10.1073/pnas.2100163118.

23. J. A. Heginbottom, J. Brown, O. Humlum, and H. Svensson, "Permafrost and Periglacial Environments," in *State of the Earth's Cryosphere at the Beginning of the 21st Century: Glaciers, Global Snow Cover, Floating Ice, and Permafrost and Periglacial Environments, USGS 1386 Series Professional Paper*, (Reston, VA: U.S. Geological Survey, 2012), A425–A496.

24. S. V. Kokelj and M. T. Jorgenson, "Advances in Thermokarst Research," *Permafrost and Periglacial Processes* 24 (2013): 108–119, https://doi.org/10.1002/ppp.1779.

25. S. V. Kokelj, J. F. Tunnicliffe, and D. Lacelle, "Landscapes and Landforms of Western Canada," (2016), https://doi.org/10.1007/978-3-319-44595-3_7.

26. B. Fox-Kemper, H. T. Hewitt, C. Xiao, et al., "Ocean, Cryosphere and Sea Level Change," in *Climate Change 2021: The Physical Science Basis. Contribution of Working Group I to the Sixth Assessment Report of the Intergovernmental Panel on Climate Change*, eds. V. Masson-Delmotte, P. Zhai, A. Pirani, et al. (Cambridge, UK and New York, NY, USA: Cambridge University Press, 2021), 1211–1362, https://doi.org/10.1017/9781009157896.011.

27. D. Lacelle, J. Bjornson, and B. Lauriol, "Climatic and Geomorphic Factors Affecting Contemporary (1950–2004) Activity of Retrogressive Thaw Slumps on the Aklavik Plateau, Richardson Mountains, NWT, Canada," *Permafrost and Periglacial Processes* 21 (2010): 1–15, https://doi.org/10.1002/ppp.666.

28. C. R. Burn and A. G. Lewkowicz, "Canadian Landform Examples—Retrogressive Thaw Slumps," *Canadian Geographic* 34 (1990): 273–276, https://doi.org/10.1111/j.1541-0064.1990.tb01092.x.

29. A. Brooker, R. H. Fraser, I. Olthof, S. V. Kokelj, and D. Lacelle, "Mapping the Activity and Evolution of Retrogressive Thaw Slumps by Tasselled Cap Trend Analysis of a Landsat Satellite Image Stack," *Permafrost and Periglacial Processes* 25 (2014): 243–256, https://doi.org/10.1002/ppp.1819.

30. F. Günther, G. Grosse, S. Wetterich, et al., "The Batagay Mega Thaw Slump, Yana Uplands, Yakutia, Russia: Permafrost Thaw Dynamics on Decadal Time Scale," (2015), in EPIC3PAST Gateways - Palaeo-Arctic Spatial and Temporal Gateways - Third International Conference and Workshop, Potsdam, Germany, 2015-05-18-2015-05-22Potsdam, TERRA NOSTRA - Schriften Der GeoUnion Alfred-Wegener-Stiftung. Presented at the PAST Gateways - Palaeo-Arctic Spatial and Temporal Gateways - Third International Conference and Workshop, TERRA NOSTRA - Schriften der GeoUnion Alfred-Wegener-Stiftung, Potsdam.

31. S. V. Kokelj, J. Kokoszka, J. van der Sluijs, et al., "Thaw-Driven Mass Wasting Couples Slopes With Downstream Systems, and Effects Propagate Through Arctic Drainage Networks," *The Cryosphere* 15 (2021): 3059–3081, https://doi.org/10.5194/tc-15-3059-2021.

32. V. V. Kunitsky, I. Syromyatnikov, L. Schirrmeister, et al., "Ice-Rich Permafrost and Thermal Denudation in the Batagay Area (Yana Upland, East Siberia)," *Earth Cryosphere (Kriosfera Zemli)* 17 (2013): 56–58.

33. D. Lacelle, A. Brooker, R. H. Fraser, and S. V. Kokelj, "Distribution and Growth of Thaw Slumps in the Richardson Mountains–Peel Plateau Region, Northwestern Canada," *Geomorphology* 235 (2015): 40–51, https://doi.org/10.1016/j.geomorph.2015.01.024.

34. M. Leibman, A. Kizyakov, Y. Zhdanova, A. Sonyushkin, and M. Zimin, "Coastal Retreat Due to Thermodenudation on the Yugorsky Peninsula, Russia During the Last Decade, Update Since 2001–2010," *Remote Sensing* 13 (2021): 4042, https://doi.org/10.3390/rs13204042.

35. V. Vadakkedath, J. Zawadzki, and K. Przeździecki, "Multisensory Satellite Observations of the Expansion of the Batagaika Crater and Succession of Vegetation in Its Interior From 1991 to 2018," *Environment and Earth Science* 79 (2020): 150, https://doi.org/10.1007/s12665-020-8895-7.

36. J. van der Sluijs, S. V. Kokelj, R. H. Fraser, J. Tunnicliffe, and D. Lacelle, "Permafrost Terrain Dynamics and Infrastructure Impacts Revealed by UAV Photogrammetry and Thermal Imaging," *Remote Sensing* 10 (2018): 1734, https://doi.org/10.3390/rs10111734.

37. J. van der Sluijs, S. V. Kokelj, and J. F. Tunnicliffe, "Allometric Scaling of Retrogressive Thaw Slumps," *The Cryosphere* 17 (2023): 4511–4533, https://doi.org/10.5194/tc-17-4511-2023.

38. S. V. Kokelj, J. Tunnicliffe, D. Lacelle, T. C. Lantz, K. S. Chin, and R. Fraser, "Increased Precipitation Drives Mega Slump Development and Destabilization of Ice-Rich Permafrost Terrain, Northwestern Canada," *Global and Planetary Change* 129 (2015a): 56–68, https://doi.org/10.1016/j.gloplacha.2015.02.008.

39. S. Shakil, S. E. Tank, S. V. Kokelj, J. E. Vonk, and S. Zolkos, "Particulate Dominance of Organic Carbon Mobilization From Thaw Slumps on the Peel Plateau, NT: Quantification and Implications for Stream Systems and Permafrost Carbon Release," *Environmental Research Letters* 15 (2020): 114019, https://doi.org/10.1088/1748-9326/abac36.

40. G. Tanski, H. Lantuit, S. Ruttor, et al., "Transformation of Terrestrial Organic Matter Along Thermokarst-Affected Permafrost Coasts in the Arctic," *Science of the Total Environment* 581–582 (2017): 434–447, https://doi.org/10.1016/j.scitotenv.2016.12.152.

41. S. V. Kokelj, J. Tunnicliffe, D. Lacelle, T. Lantz, and R. Fraser, "Retrogressive Thaw Slumps: From Slope Process to the Landscape Sensitivity of Northwestern Canada," (2015b), Presented at the GeoQuebec 2015 Conference, Quebec City, Quebec, Canada.

42. J. B. Murton and C. K. Ballantyne, "Periglacial and permafrost ground models for Great Britain," in *Engineering Geology and Geomorphology of Glaciated and Periglaciated Terrains – Engineering Group Working Party Report*, vol. 28, eds. J. S. BGriffiths and C. J. Martin (Geological Society, London, Engineering Geology Special Publications, 2017), 501–597, https://doi.org/10.1144/EGSP28.5.

43. C. Mu, F. Zhang, M. Mu, X. Chen, Z. Li, and T. Zhang, "Organic Carbon Stabilized by Iron During Slump Deformation on the Qinghai-Tibetan Plateau," *Catena* 187 (2020): 104282, https://doi.org/10.1016/j.catena.2019.104282.

44. C. C. Mu, T. J. Zhang, Q. Zhao, et al., "Soil Organic Carbon Stabilization by Iron in Permafrost Regions of the Qinghai-Tibet Plateau," *Geophysical Research Letters* 43 (2016): 10286–10294, https://doi.org/10.1002/2016GL070071.

45. S. Shakil, S. E. Tank, J. E. Vonk, and S. Zolkos, "Low Biodegradability of Particulate Organic Carbon Mobilized From Thaw Slumps on the Peel Plateau, NT, and Possible Chemosynthesis and Sorption Effects," *Biogeosciences* 19 (2022): 1871–1890, https://doi.org/10.5194/bg-19-1871-2022.

46. M. Thomas, A. Monhonval, C. Hirst, et al., "Evidence for Preservation of Organic Carbon Interacting With Iron in Material Displaced From Retrogressive Thaw Slumps: Case Study in Peel Plateau, Western Canadian Arctic," *Geoderma* 433 (2023): 116443, https://doi.org/10.1016/j.geoderma.2023.116443.

47. J. M. Lavallee, J. L. Soong, and M. F. Cotrufo, "Conceptualizing Soil Organic Matter Into Particulate and Mineral-Associated Forms to Address Global Change in the 21st Century," *Global Change Biology* 26 (2020): 261–273, https://doi.org/10.1111/gcb.14859.

48. P. García-Palacios, M. A. Bradford, I. Benavente-Ferraces, et al., "Dominance of Particulate Organic Carbon in Top Mineral Soils in Cold Regions," *Nature Geoscience* 1–6 (2024): 145–150, https://doi.org/10.1038/s41561-023-01354-5.

49. R. G. Keil and L. M. Mayer, "Mineral Matrices and Organic Matter," in *Treatise on Geochemistry*, Second ed., eds. H. D. Holland and K. K. Turekian (Oxford: Elsevier, 2014), 337–359, https://doi.org/10.1016/B978-0-08-095975-7.01024-X.

50. M. Kleber, K. Eusterhues, M. Keiluweit, C. Mikutta, R. Mikutta, and P. S. Nico, "Mineral–Organic Associations: Formation, Properties, and Relevance in Soil Environments," in *Advances in Agronomy*, ed. D. L. Sparks (Delaware, USA: Department of Plant and Soil Sciences University of Delaware Newark, 2015), 1–140, https://doi.org/10.1016/bs.agron.2014.10.005.

51. K. Lalonde, A. Mucci, A. Ouellet, and Y. Gélinas, "Preservation of Organic Matter in Sediments Promoted by Iron," *Nature* 483 (2012): 198–200, https://doi.org/10.1038/nature10855.

52. M. W. I. Schmidt, M. S. Torn, S. Abiven, et al., "Persistence of Soil Organic Matter as an Ecosystem Property," *Nature* 478 (2011): 49–56, https://doi.org/10.1038/nature10386.

53. K. Dutta, E. A. G. Schuur, J. C. Neff, and S. A. Zimov, "Potential Carbon Release From Permafrost Soils of Northeastern Siberia," *Global Change Biology* 12 (2006): 2336–2351, https://doi.org/10.1111/j.1365-2486.2006.01259.x.

54. C. W. Mueller, J. Rethemeyer, J. Kao-Kniffin, S. Löppmann, K. M. Hinkel, and J. G. Bockheim, "Large Amounts of Labile Organic Carbon in Permafrost Soils of Northern Alaska," *Global Change Biology* 21 (2015): 2804–2817, https://doi.org/10.1111/gcb.12876.

55. J. A. Salvadó, T. Tesi, A. Andersson, et al., "Organic Carbon Remobilized From Thawing Permafrost Is Resequestered by Reactive Iron on the Eurasian Arctic Shelf," *Geophysical Research Letters* 42 (2015): 8122–8130, https://doi.org/10.1002/2015GL066058.

56. F. Courchesne and M.-C. Turmel, "Extractable Al, Fe, Mn, and Si," in *Soil Sampling and Methods of Analysis. Canadian Society of Soil Science*, eds. M. R. Carter and E. G. Gregorich ([Pinawa, Manitoba]: Boca Raton, FL: CRC Press, 2008), 307–315.

57. M. von Lützow, I. Kögel-Knabner, K. Ekschmitt, et al., "Stabilization of Organic Matter in Temperate Soils: Mechanisms and Their Relevance Under Different Soil Conditions—A Review," *European Journal of Soil Science* 57 (2006): 426–445, https://doi.org/10.1111/j.1365-2389.2006.00809.x.

58. I. Kögel-Knabner, G. Guggenberger, M. Kleber, et al., "Organo-Mineral Associations in Temperate Soils: Integrating Biology, Mineralogy, and Organic Matter Chemistry," *Journal of Plant Nutrition and Soil Science* 171 (2008): 61–82, https://doi.org/10.1002/jpln.200700048.

59. J. B. Murton, T. Opel, P. Toms, et al., "A Multimethod Dating Study of Ancient Permafrost, Batagay Megaslump, East Siberia," *Quaternary Research* 105 (2022): 1–22, https://doi.org/10.1017/qua.2021.27.

60. J. Obu, S. Westermann, A. Kääb, and A. Bartsch, *Ground Temperature Map, 2000–2016, Northern Hemisphere Permafrost* (Bremerhaven: Alfred Wegener Institute, Helmholtz Centre for Polar and Marine Research, 2018).

61. L. L. Jongejans, T. Opel, J. Courtin, et al., "Batagay Outcrop Sampling," in *Russian-German Cooperation: Expeditions to Siberia in 2019, Reports on Polar and Marine Research*, eds. M. Fuchs, D. Bolshiyanov, M. Grigoriev, et al. (Bremerhaven, Germany: Alfred Wegener Institute for Polar and Marine Research, 2021), 155–210.

62. G. N. Savvinov, P. P. Danilov, A. A. Petrov, V. S. Makarov, V. S. Boeskorov, and S. E. Grigoriev, "Environmental Problems of the Verkhoyansky Region. Vestnik of North-Eastern Federal University," *Earth Science* 6 (2018): 18–33, https://doi.org/10.25587/SVFU.2018.68.21798.

63. A. I. Kizyakov, S. Wetterich, F. Günther, et al., "Landforms and Degradation Pattern of the Batagay Thaw Slump, Northeastern Siberia," *Geomorphology* 420 (2023): 108501, https://doi.org/10.1016/j.geomorph.2022.108501.

64. J. Murton, T. Opel, S. Wetterich, et al., "Batagay Megaslump: A Review of the Permafrost Deposits, Quaternary Environmental History, and Recent Development," *Permafrost and Periglacial Processes* 34 (2023): 399–416, https://doi.org/10.1002/ppp.2194.

65. W. Köppen, "Die Wärmezonen der Erde, Nach der Dauer der Heissen, gemässigten Und Kalten Zeit Und Nach der Wirkung der Wärme Auf Die Organische Welt Betrachtet (the Thermal Zones of the Earth According to the Duration of Hot, Moderate and Cold Periods and to the Impact of Heat on the Organic World)," *Meteorologische Zeitschrift* 20 (1884): 351–360, https://doi.org/10.1127/0941-2948/2011/105.

66. J. Strauss, S. Laboor, L. Schirrmeister, et al., "Circum-Arctic Map of the Yedoma Permafrost Domain," *Frontiers in Earth Science* 9 (2021b): 758360, https://doi.org/10.3389/feart.2021.758360.

67. R. Ravansari, S. C. Wilson, and M. Tighe, "Portable X-Ray Fluorescence for Environmental Assessment of Soils: Not Just a Point and Shoot Method," *Environment International* 134 (2020): 105250, https://doi.org/10.1016/j.envint.2019.105250.

68. A. Monhonval, E. Mauclet, B. Pereira, et al., "Mineral Element Stocks in the Yedoma Domain: A Novel Method Applied to Ice-Rich Permafrost Regions," *Frontiers in Earth Science* 9 (2021a): 773, https://doi.org/10.3389/feart.2021.703304.

69. L. L. Jongejans, K. Mangelsdorf, C. Karger, and J. Strauss, *Alkane, Fatty Acid, Total (Organic) Carbon and Nitrogen Distribution in Ancient Permafrost Deposits at the Batagay Megaslump, East Siberia*, [dataset bundled publication]. PANGAEA, (2022b), https://doi.org/10.1594/PANGAEA.950124.

70. T. Rennert, "Wet-Chemical Extractions to Characterise Pedogenic Al and Fe Species—A Critical Review," *Soil Research* 57 (2019): 1–16, https://doi.org/10.1071/SR18299.

71. C. L. Bascomb, "Distribution of Pyrophosphate-Extractable Iron and Organic Carbon in Soils of Various Groups," *Journal of Soil Science* 19 (1968): 251–268, https://doi.org/10.1111/j.1365-2389.1968.tb01538.x.

72. R. L. Parfitt and C. W. Childs, "Estimation of Forms of Fe and Al—A Review, and Analysis of Contrasting Soils by Dissolution and Mossbauer Methods," *Soil Research* 26 (1988): 121–144, https://doi.org/10.1071/sr9880121.

73. E. Jeanroy and B. Guillet, "The Occurrence of Suspended Ferruginous Particles in Pyrophosphate Extracts of some Soil Horizons," *Geoderma* 26 (1981): 95–105, https://doi.org/10.1016/0016-7061(81)90078-1.

74. K. Kaiser and W. Zech, "Defects in Estimation of Aluminum in Humus Complexes of Podzolic Soils by Pyrophosphate Extraction," *Soil Science* 161 (1996): 452–458, https://doi.org/10.1097/00010694-199607000-00005.

75. L. C. Blakemore, P. L. Searle, and B. K. Daly, "Methods for Chemical Analysis of Soils." New Zealand Soil Bur. Scientific Rep., Second Revision 10A, (1981), https://doi.org/10.7931/DL1-SBSR-10A.

76. B. K. Daly, "Identification of Podzols and Podzolised Soils in New Zealand by Relative Absorbance of Oxalate Extracts of A and B Horizons," *Geoderma* 28 (1982): 29–38, https://doi.org/10.1016/0016-7061(82)90038-6.

77. J. Strauss, L. Schirrmeister, G. Grosse, et al., "The Deep Permafrost Carbon Pool of the Yedoma Region in Siberia and Alaska," *Geophysical Research Letters* 40 (2013): 6165–6170, https://doi.org/10.1002/2013GL058088.

78. R Core Team, "R: A Language and Environment for Statistical Computing," (2019), Vienna, Austria.

79. J. L. Hintze and R. D. Nelson, "Violin Plots: A Box Plot-Density Trace Synergism," *The American Statistician* 52 (1998): 181, https://doi.org/10.2307/2685478.

80. R. McGill, J. W. Tukey, and W. A. Larsen, "Variations of Box Plots," *The American Statistician* 32 (1978): 12–16, https://doi.org/10.2307/2683468.

81. R. Wagai and L. M. Mayer, "Sorptive Stabilization of Organic Matter in Soils by Hydrous Iron Oxides," *Geochimica et Cosmochimica Acta* 71 (2007): 25–35, https://doi.org/10.1016/j.gca.2006.08.047.

82. J. B. Murton, T. Goslar, M. E. Edwards, et al., "Palaeoenvironmental Interpretation of Yedoma Silt (Ice Complex) Deposition as Cold-Climate Loess, Duvanny Yar, Northeast Siberia," *Permafrost and Periglacial Processes* 26 (2015): 208–288, https://doi.org/10.1002/ppp.1843.

83. L. Schirrmeister, V. Kunitsky, G. Grosse, et al., "Sedimentary Characteristics and Origin of the Late Pleistocene Ice Complex on North-East Siberian Arctic Coastal Lowlands and Islands—A Review," *Quaternary International, Timing and Vegetation History of Past Interglacials in Northern Eurasia* 241 (2011): 3–25, https://doi.org/10.1016/j.quaint.2010.04.004.

84. J. Strauss, L. Schirrmeister, G. Grosse, et al., "Deep Yedoma Permafrost: A Synthesis of Depositional Characteristics and Carbon Vulnerability," *Earth-Science Reviews* 172 (2017): 75–86, https://doi.org/10.1016/j.earscirev.2017.07.007.

85. K. Ashastina, L. Schirrmeister, M. Fuchs, and F. Kienast, "Palaeoclimate Characteristics in Interior Siberia of MIS 6–2: First Insights From the Batagay Permafrost Mega-Thaw Slump in the Yana Highlands," *Climate of the Past* 13 (2017): 795–818, https://doi.org/10.5194/cp-13-795-2017.

86. N. G. Pisias, D. G. Martinson, T. C. Moore, et al., "High Resolution Stratigraphic Correlation of Benthic Oxygen Isotopic Records Spanning the Last 300,000 Years," *Marine Geology* 56 (1984): 119–136, https://doi.org/10.1016/0025-3227(84)90009-4.

87. K. Ashastina, S. Kuzmina, N. Rudaya, et al., "Woodlands and Steppes: Pleistocene Vegetation in Yakutia's Most Continental Part Recorded in the Batagay Permafrost Sequence," *Quaternary Science Reviews* 196 (2018): 38–61, https://doi.org/10.1016/j.quascirev.2018.07.032.

88. T. Opel, J. B. Murton, S. Wetterich, et al., "Past Climate and Continentality Inferred From Ice Wedges at Batagay Megaslump in the Northern Hemisphere's most Continental Region, Yana Highlands, Interior Yakutia," *Climate of the Past* 15 (2019): 1443–1461, https://doi.org/10.5194/cp-15-1443-2019.

89. O. P. Mehra and M. L. Jackson, "Iron Oxide Removal from Soils and Clays by a Dithionite-Citrate System Buffered With Sodium Bicarbonate," *Clays and Clay Minerals* 7 (1958): 317–327, https://doi.org/10.1346/CCMN.1958.0070122.

90. S. W. Poulton and D. E. Canfield, "Development of a Sequential Extraction Procedure for Iron: Implications for Iron Partitioning in Continentally Derived Particulates," *Chemical Geology* 214 (2005): 209–221, https://doi.org/10.1016/j.chemgeo.2004.09.003.

91. N. Gentsch, R. Mikutta, O. Shibistova, et al., "Properties and Bioavailability of Particulate and Mineral-Associated Organic Matter in Arctic Permafrost Soils, Lower Kolyma Region, Russia," *European Journal of Soil Science* 66 (2015): 722–734, https://doi.org/10.1111/ejss.12269.

92. A. Monhonval, J. Strauss, E. Mauclet, et al., "Iron Redistribution Upon Thermokarst Processes in the Yedoma Domain," *Frontiers in Earth Science* 9 (2021b), 703339, https://doi.org/10.3389/feart.2021.703339.

93. J. Martens, C. W. Mueller, P. Joshi, et al., "Stabilization of Mineral-Associated Organic Carbon in Pleistocene Permafrost," *Nature Communications* 14 (2023): 2120, https://doi.org/10.1038/s41467-023-37766-5.

94. M. S. Patzner, C. W. Mueller, M. Malusova, et al., "Iron Mineral Dissolution Releases Iron and Associated Organic Carbon During Permafrost Thaw," *Nature Communications* 11 (2020): 6329, https://doi.org/10.1038/s41467-020-20102-6.

95. A. Monhonval, E. Mauclet, C. Hirst, et al., "Mineral Organic Carbon Interactions in Dry Versus Wet Tundra Soils," *Geoderma* 436 (2023): 116552, https://doi.org/10.1016/j.geoderma.2023.116552.

96. L. Schirrmeister, E. Dietze, H. Matthes, et al., "The Genesis of Yedoma Ice Complex Permafrost—Grain-Size Endmember Modeling Analysis From Siberia and Alaska," *E&G Quaternary Science Journal* 69 (2020): 33–53, https://doi.org/10.5194/egqsj-69-33-2020.

97. L. Schirrmeister, D. Froese, V. Tumskoy, G. Grosse, and S. Wetterich, "Yedoma: Late Pleistocene Ice-Rich Syngenetic Permafrost of Beringia," in *Encyclopedia of Quaternary Science* (Second Edition), eds. S. A. Elias and C. J. Mock (Amsterdam, The Netherlands: Elsevier, 2013), 542–552, https://doi.org/10.1016/B978-0-444-53643-3.00106-0.

98. A. Monhonval, J. Strauss, M. Thomas, et al., "Thermokarst Processes Increase the Supply of Stabilizing Surfaces and Elements (Fe, Mn, Al, and Ca) for Mineral–Organic Carbon Interactions," *Permafrost and Periglacial Processes* 33 (2022): 452–469, https://doi.org/10.1002/ppp.2162.

99. M. Fritz, T. Opel, G. Tanski, et al., "Dissolved Organic Carbon (DOC) in Arctic Ground Ice," *The Cryosphere* 9 (2015): 737–752, https://doi.org/10.5194/tc-9-737-2015.

100. A. I. Kizyakov, M. V. Korotaev, S. Wetterich, et al., "Characterizing Batagay Megaslump Topography Dynamics and Matter Fluxes at High Spatial Resolution Using a Multidisciplinary Approach of Permafrost Field Observations, Remote Sensing and 3D Geological Modeling," *Geomorphology* 455 (2024): 109183, https://doi.org/10.1016/j.geomorph.2024.109183.

101. J. E. Vonk, P. J. Mann, K. L. Dowdy, et al., "Dissolved Organic Carbon Loss From Yedoma Permafrost Amplified by Ice Wedge Thaw," *Environmental Research Letters* 8 (2013b): 035023, https://doi.org/10.1088/1748-9326/8/3/035023.

102. C. R. Burn and P. A. Friele, "Geomorphology, Vegetation Succession, Soil Characteristics and Permafrost in Retrogressive Thaw Slumps Near Mayo, Yukon Territory," *Arctic* 42 (1989): 31–40.

103. S. V. Kokelj, T. C. Lantz, J. Kanigan, S. L. Smith, and R. Coutts, "Origin and Polycyclic Behaviour of Tundra Thaw Slumps, Mackenzie Delta Region, Northwest Territories, Canada," *Permafrost and Periglacial Processes* 20 (2009): 173–184, https://doi.org/10.1002/ppp.642.

Supporting Information

Additional supporting information can be found online in the Supporting Information section.